Geometry of vegetation patterns: understanding patterns in dryland ecosystems and beyond

Jaïbi, O.

2

Multi-stability of model and real dryland ecosystems through spatial self-organization

Spatial self-organization of dryland vegetation constitutes one of the most promising indicators for an ecosystem's proximity to desertification. This insight is based on studies of reaction-diffusion models that reproduce visual characteristics of vegetation patterns observed on aerial photographs. However, until now, the development of reliable early warning systems has been hampered by the lack of more in-depth comparisons between model predictions and real ecosystem patterns. In this chapter, we combined topographical data, (remotely sensed) optical data and in-situ biomass measurements from two sites in Somalia to generate a multi-level description of dryland vegetation patterns. We performed an in-depth comparison between these observed vegetation pattern characteristics and predictions made by the extended-Klausmeier model for dryland vegetation patterning. Consistent with model predictions, we found that for a given topography, there is multi-stability of ecosystem states with different pattern wavenumbers. Furthermore, observations corroborated model predictions regarding the relationships between pattern wavenumber, total biomass and maximum biomass. In contrast, model predictions regarding the role of slope angles were not corroborated by the empirical data, suggesting that inclusion of small-scale topographical heterogeneity is a promising avenue for future model development. Our findings suggest that patterned dryland ecosystems may be more resilient to environmental change than previously anticipated, but this enhanced resilience crucially depends on the adaptive capacity of vegetation patterns.

1 Introduction

A key aim of ecological modeling is to generate an understanding of the mechanisms driving observed patterns [99]. A significant challenge in this pursuit, however, is that multiple alternative processes may generate the same emergent outcome [48, 70, 99, 153], a phenomenon also referred to as equifinality [93, 94]. As a result, modeling efforts may reveal that a particular ecological pattern can be explained by a suite of alternative driver mechanisms. Therefore, a match between a pattern simulated with a mechanistic model and a pattern observed in a real ecosystem may only constitute limited support for the modeled mechanism being its true driver [70, 93, 94].

Pattern-oriented modeling [69, 70] aims to address the challenge of equifinality of alternative model formulations. In this approach, model assessment is based on the degree to which the output corresponds to observed patterns. A distinction is made between strong and weak patterns. Strong patterns are the dominant emergent features a model should reproduce, such as the cycles within predator and prey population sizes, or a spatial distribution of vegetation patches [69, 94]. Weak patterns are typically qualitative relationships, such as the existence of a population over a specific timespan, or a positive association between one state variable and another [69, 94]. Rather than comparing model output to a single strong pattern, additional comparisons to multiple weak patterns, at different scales or levels of organization, provide more power to model validation and selection procedures [69, 70, 94].

A specific type of ecological patterns that has received considerable attention is regular spatial patterning of sessile biota [126]. On flat terrain, the reported patterns are gaps, labyrinths, and spots [124, 161]. On sloping grounds banded patterns form, their regular spacing enabling a description of the characteristic band-inter-band period and wavenumber. Evidence is accumulating that these patterns are self-organized, meaning that the larger-scale patterning is driven by internal ecosystem processes operating at smaller scales [125, 126]. The crucial component in this self-organization process is a long-range negative effect of biota on itself, either directly or through modulation of resource availability. In cases where this long-range negative feedback is coupled to a locally positive feedback, the mechanism creating pattern formation may be linked to the existence of alternative stable states, as well as the possibility of so-called catastrophic shifts between these states [125]. This phenomenon has been most prominently studied in (semi-)arid ecosystems, where decreases in resource availability or increases in grazing pressure may trigger catastrophic shifts from vegetated states to desert states without vegetation [103, 115, 127]. In this context, the formation of regular spatial vegetation patterns may indicate proximity to a threshold of catastrophic change [125].

There is a long tradition in the scientific literature of explaining regular spatial patterning with reaction-diffusion models [29, 114, 150]. In line with this work, a variety of reaction-diffusion models has been applied to investigate self-organization in (semi-)arid ecosystems [62, 90, 124, 161]. Despite the broad support for the findings obtained with these models and their implications for (semi-)arid ecosystem functioning, comparisons of model results with empirical data have mainly been limited to comparison of a single strong pattern, namely the spatial distribution of vegetation patches. Until now, the few studies considering additional weak patterns have shown that reaction-diffusion model simulations successfully reproduce associations between pattern shape and aridity, and associations between pattern shape and slope of the terrain [34]. In addition, models that account for sloped terrain also seem to capture the observed migration of the location of banded patterns in uphill direction [33]. Despite these promising agreements between model results and empirical data, a more systematic comparison between model results and data, based on multiple patterns at different levels of organization [69, 70], was still lacking.

Advanced model analyses that have recently been applied to ecological models have yielded a number of findings which, when confronted with high quality remote sensing products, makes a more systematic comparison possible. More specifically, recent theoretical studies have shown that for a given environmental condition (i.e., a given parameter combination), not a single ecosystem state, but multiple ecosystem states with patterns spanning a range of wavenumbers may be stable, hence observable [143, 146, 155]. The range of observable patterns, across a range of environmental conditions forms a bounded region in (parameter,wavenumber)-space. This region is referred to as the Busse balloon, after F.H. Busse, who studied similar phenomena in the field of fluid dynamics [18]. Although the patterned ecosystem states in the Busse balloon are defined by their wavenumber, other properties, like migration speed and spatially averaged biomass, have also been studied [138] and are suggested to depend on the position of a system within the Busse balloon. These theoretical findings provide multiple additional weak patterns that can be compared to empirical data, providing opportunities for more powerful tests of the validity of the developed reaction-diffusion models to describe dryland ecosystems.

The aim of this study was to confront theoretical findings regarding pattern wavenumber, biomass and migration speed with the same pattern properties derived from aerial imagery and remote sensing products of banded vegetation patterns in the Horn of Africa, a location with prominent undisturbed presence of vegetation pattern formation. Hence, a multi-level comparison between theory and data in line with the pattern-oriented modeling approach was conducted [69, 70, 94].

2 Theory

2.1 Model description

Multiple reaction-diffusion models of dryland vegetation dynamics include a mechanism in which vegetation acts as an ecosystem engineer, locally increasing the influx of available water [62, 90, 124, 161]. Despite the different nuances between these models, a number of predictions can be robustly derived from these frameworks. One of the simplest of these ecosystem models – and the archetype considered in this article – is an extended version of the dryland ecosystem model by Klausmeier [90, 155], which we will refer to as the extended-Klausmeier model. This model describes the interaction between water, w, and plant biomass, n. A non-dimensional version of this model is used for the purposes of this article. A dimensional version of the model and the physical meaning of its parameters can be found in Appendix 2.A. The model is given by the following equations

$$\begin{cases} \dfrac{\partial w}{\partial t} &= e\dfrac{\partial^2 w}{\partial x^2} + \dfrac{\partial (vw)}{\partial x} + a - w - wn^2, \\ \dfrac{\partial n}{\partial t} &= \dfrac{\partial^2 n}{\partial x^2} - mn + wn^2. \end{cases} \tag{2.1}$$

The reaction terms model the change in water as a combined effect of rainfall ($+a$), evaporation ($-w$) and uptake by plants ($-wn^2$). The change of plant biomass comes from mortality ($-mn$) and plant growth ($+wn^2$). Dispersion by plants is modeled as diffusion and the movement of water as a combined effect of diffusion and advection. The latter is due to gradients in the terrain, which are proportional to the slope parameter v.

2.2 Theoretical outcomes

1 Multi-stability of patterned states

Reaction-advection-diffusion equations in general – and the extended-Klausmeier model in particular – exhibit a vast variety of spatial patterns [96, 117]. However, not all feasible patterns are stable solutions of these models. Which patterned states are stable (hence, observable) depends on the combination of the model parameters. For regular patterns, the concept of the Busse balloon can help to illustrate this dependency [18]. A Busse balloon is a model dependent shape in the (parameter,wavenumber)-space that indicates all combinations of parameter and wavenumber that represent stable solutions of the model. If, for a given set of model parameters, a wavenumber k lies within the Busse balloon, then regular patterns with wavenumber k are observable. So, in measurements, all (non-transient) patterns are expected to be present in the Busse balloon.

Typically, the Busse balloon is a high-dimensional structure due to the number of parameters in a system. Therefore, usually, only one parameter is varied when a Busse balloon is visualized. This produces a 2D-slice of the full Busse balloon. In the context of desertification research, the straightforward choice would be to vary the rainfall [146]. However, mean annual rainfall was relatively constant in our study sites during the observation period considered. Instead, topography (i.e., the slope gradient) comprised the main source of environmental variation within our study areas. Thus, relevant theoretical predictions for our study sites can be generated by varying the slope parameter v (while keeping rainfall constant). Here, we present two of such 2D-Busse balloon slices for the extended-Klausmeier model (Figure 2.1), which were constructed by tracking the boundary of the Busse balloon using numerical continuation methods [122, 141, 143, 146]. The shaded region in these figures indicates the combinations of pattern wavenumber k and slope v for which stable solutions exist. Thus, the model shows multi-stability; a given slope v can sustain a continuous range of wavenumbers k. That is, knowing all current parameter values of a system is not enough to predict the pattern, but only gives a range of possible wavenumbers – as indicated by the Busse balloon. For patterns with wavenumbers above this range, there are too few resources to sustain all bands; below this range, there is an abundance of resources that leads to the formation of additional vegetation bands. It is in general not possible to predict which of these wavenumbers is selected at a specific location; small changes in the (entire) history of environmental changes can have large impacts on the wavenumber that is currently selected [138, 140]. To understand these hysteretic dynamics, it is vital to acknowledge that model patterns do not change their wavenumber unless they have to [141, 146]: if an environmental change forces the system outside of the Busse balloon, the current pattern has become unstable, and will need to adapt into a new pattern that is again stable – thus part of the Busse balloon. During this (fast) adaption, only part of the vegetation bands are lost, while the remaining bands increase in volume; these adaptations thus have limited effect on the total biomass in the system [146]. Hence, multiple wavenumber adaptations are expected to occur after each other that will, gradually, lead to a complete desertification of the system [146]. Both the moment of a destabilization and the then occurring wavenumber adaption can be vastly different depending on (historical) environmental conditions [11, 138, 140]. Thus, indeed, precisely which wavenumber k gets selected at each of these destabilizations is difficult to predict.

Numerical simulations help to get an insight in the kind of wavenumber distribution one ought to expect in observations. To illustrate the typical spread in wavenumber, a total of 200 simulations on a flat terrain ($v = 0$) were run, where the rainfall parameter was slowly decreased from $a = 3$ to $a = 0.5$. The initial configurations for these runs were chosen randomly, but close to the equilibrium state of uniform biomass before the onset of patterns (between 90% and 110%

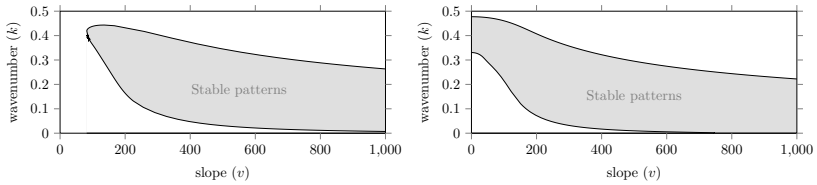

(a) $a = 3.0$, $m = 0.45$ and $e = 500$. **(b)** $a = 2.5$, $m = 0.45$ and $e = 500$.

Figure 2.1: (*slope*, *wavenumber*)-Busse balloon slices for the extended-Klausmeier model for two different values of the rainfall parameter a. A banded pattern solution to the extended-Klausmeier model with slope v and wavenumber k is stable if the (v, k)-combination lies inside the Busse balloon. This indicates that a wide spread of (v, k)-combinations yields stable banded patterns. The latter are therefore expected for a broad range of wavenumbers – and not for specific (v, k)-choices only. The shape of a Busse balloon can change between models and between parameter values. This is illustrated in the figures which were computed for different a-values.

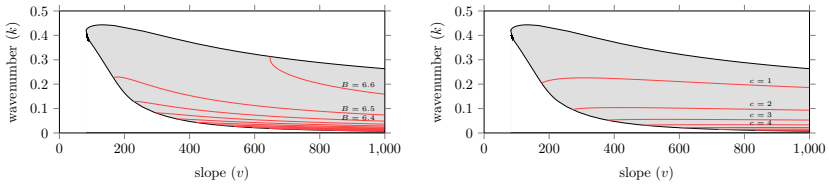

(a) Total biomass contours. **(b)** Migration speed contours

Figure 2.2: (*slope*, *wavenumber*)-Busse balloon slices for the extended Klausmeier model that include contours for the total biomass (per area) B (a) and the migration speed c (b). Biomass (per area) is positively correlated with both wavenumber k and slope v; the migration speed is negatively correlated with the wavenumber k. Model parameters used: $a = 3$, $m = 0.45$, $e = 500$.

of the uniform vegetated equilibrium state). At the end of each simulation – after several pattern selections – the wavenumber of the remaining pattern was measured. This gives a snapshot of the wavenumber distribution, similar to the snapshots acquired from observations. Note that a similar experiment was done before, albeit on a much smaller scale [141]. The histogram of the resulting wavenumbers is shown in Figure 2.3. It shows a substantial spread, which goes from a wavenumber of 0.08 to 0.16 (a difference of 100%).

2 Biomass & migration speed

Besides a wavenumber, each ecosystem state also has a specific biomass and a specific pattern migration speed. The biomass of regular patterned states has been studied using numerical simulations [146] and more general formulas have

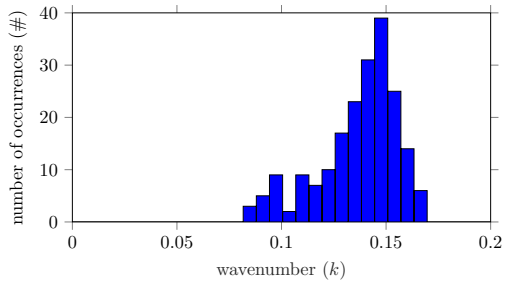

Figure 2.3: Histogram demonstrating a spread in wavenumber (k) at the end of 200 simulations of the extended-Klausmeier model on a flat terrain ($v = 0$) with model parameters $e = 500$ and $m = 0.45$. These simulations had a random initial configuration close to a stable fully vegetated state. A climate change was simulated by decreasing the rainfall parameter a linearly from 3 to 0.5 over the course of 10^5 time unit, causing several pattern selections and corresponding changes in wavenumber.

been derived for patterns with small wavenumber [11]. Both indicate that the biomass (per unit area) is positively correlated with both the wavenumber k of the pattern and the slope parameter v [146]; see also Figure 2.2a. This has a physical interpretation: both steeper slopes and higher wavenumbers (lower wavelengths) reduce the time it takes for water to reach vegetation bands, and thereby reduce water losses during the transportation process. As a result, the vegetation will be able to harvest water from the uphill inter-bands more effectively. The biomass per wavelength is also of interest. The same studies indicate that the band biomass (per wavelength) is increased when the wavenumber k is decreased and when the slope v is increased. Hence, vegetation bands are expected to have more biomass when other vegetation is farther away, because of the larger (upslope) inter-band area water can be collected from.

The theoretical predictions for migration speed (of a pattern's location) are a bit more subtle. For terrains with a constant slope, numerical simulations have been done [136, 139] and general formulas have been determined for patterns with small wavenumber [11, 133]. In these idealized limit cases, migration speed is negatively correlated with wavenumber k and positively correlated with slope v. However, beyond these idealizations, numerical computations show the contour lines are slightly humped, see Figure 2.2b. This indicates a (slightly) negative correlation between speed and slope v for large slopes.

2.3 Testable predictions

The theoretical findings in this section lead to predictions that can be confronted with the field data. First of all, the model possesses a Busse balloon, which should lead to a wide spread in observable pattern wavenumbers (Figures 2.1 and 2.3). Moreover, biomass and migration speed are affected by pattern

wavenumber. The biomass (per unit area) is expected to be positively correlated with both the wavenumber and the slope of the terrain (Figure 2.2a). Migration speed is expected to decrease as a function of pattern wavenumber; the effect of slope on the migration speed is context-specific, as it can be either positive or negative depending on the specific topographical and environmental conditions (Figure 2.2b).

3 Data acquisition & processing

For this comparison study, two sites were selected in Somalia. The first one (8°0′14″ to 8°15′11″N; 47°11′54″ to 47°31′4″E) is located in the Haud pastoral region, which will be referred to as the 'Haud' site. The other site (9°18′49″ to 9°34′34″N; 48°8′15″ to 48°43′15″E) is located in the Sool-Plateau pastoral area and will be called the 'Sool' site. Both sites mainly exhibit banded vegetation and have ground slopes ranging from 0% to 1%. Vegetation mainly constitutes of perennial grasses, which typically have an average lifetime of 1-7 years [19, 95, 171]. A more detailed description of these sites can be found in Appendix 2.B; a map with the location of these sites along with the mean annual rainfall in these areas is shown in Figure 2.D.1.

To study the pattern properties in these study areas, each site was divided into square windows (of size $750m \times 750m$ for the Haud site and of size $1010m \times 1010m$ for the Sool site). As has been done in previous studies, the type of pattern (e.g. bare soil, banded vegetation), along with its wavenumber, was determined using spectral analysis [7, 27, 34, 118]. Only those windows were kept that exhibited banded vegetation with a wavenumber that could be determined with enough certainty (i.e., between 0.4 and 2.5 cycles per $100m$). Moreover, windows with a too large curvature were ignored, because the theoretical predictions only apply to terrains with a constant slope. To obtain data on the migration speed of the banded vegetation, a cross-spectral analysis was performed, along the lines of previous studies [8, 33, 66]. A more in-depth explanation of the processing steps can be found in Appendix 2.D.

The topographical data used in this article were derived from the Advanced Land Observation Satellite (ALOS) World 3D (AW3D) digital raster elevation model; biomass data for the Haud site have been retrieved from a recently made map on (above-ground) biomass of African savannahs and woodlands [15] (no reliable data for the Sool site was available). Finally, optical data was acquired from various sources: three multi-spectral WorldView-2 images were mosaicked and used as reference for the Haud site; a panchromatic Ikonos "Geo" Imagery was acquired for the same site. For the Sool site, six WorldView-2 images were used and a panchromatic Satellite Pour l'Observation de la Terre (SPOT) 4 image preprocessed to level 2A was used as reference layer (©Cnes 2004 – Spot Image

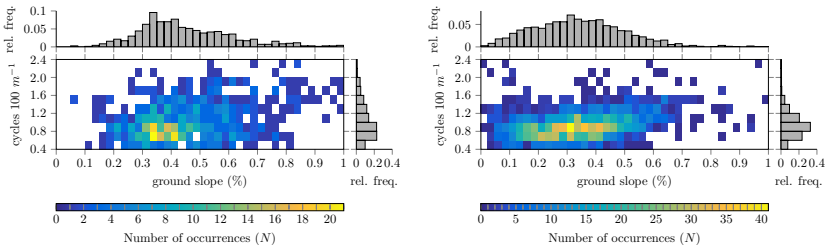

(a) Frequency distribution for the Haud site **(b)** Frequency distribution for the Sool site

Figure 2.4: Frequency distribution of banded patterns as function of ground slope and wavenumber (number of cycles per 100m) for the Haud site (a) and Sool site (b). The distribution on the right indicates the relative frequency of banded vegetation with corresponding wavenumber. The color gradient indicates the amount of windows (N).

distribution). Moreover, two $7\mu m$ digitized panchromatic declassified Corona spy satellite image, national intelligence reconnaissance system, available from the US Geological Survey, were obtained for the Haud and the Sool sites. More information about these data sets can be found in Appendix 2.C.

4 Results

Empirical Busse balloon

The most prominent pattern property studied in this article is the pattern wavenumber, which was derived from aerial imagery. The resulting distribution of wavenumbers is reported in Figure 2.4 (a map with the spatial distribution of wavenumbers over the study sites is shown in Figure 2.D.2). These figures show the number of windows that have a particular slope-wavenumber combination. Also given is the relative frequency that indicates the spread of wavenumbers across all windows. The data display banded vegetation with wavenumbers roughly between 0.4 and 2.0 cycles per $100m$. Importantly, this large spread is present for all of the ground slope values which had a representative sample size and could not be explained by present heterogeneities in elevation or rainfall. This shows that for a given environmental condition not a single wavenumber pattern, but rather multiple patterns spanning a sizable range of wavenumbers are observable. Additionally, measurements used to determine the migration speed show barely any changes in wavenumber over the scope of 39 years (consistent with [66]), indicating that these patterns are in fact quite stable. Therefore, the observations are in agreement with the existence of a Busse balloon in the real ecosystem.

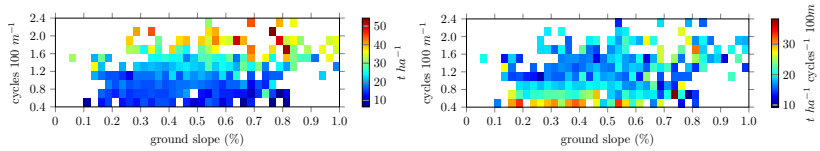

(a) Biomass per unit area (Haud site) **(b)** Biomass per period (Haud site)

Figure 2.5: Biomass distribution per area (a) and per period (b) as a function of ground slope and wavenumber (cycles per 100m) for the Haud site. The color gradient indicates the amount of biomass measured for a particular (*slope*, *wavenumber*)-combination.

Biomass and migration speed

The processed biomass data for the Haud site is shown in Figure 2.5. In Figure 2.5a the relation between biomass per area (in $t\ ha^{-1}$) is plotted against the ground slope and the wavenumber. From the same data the biomass per period is computed – which is biomass per area divided by the window's wavenumber. The resulting plot is given in Figure 2.5b. The measurements of biomass show agreement with theoretical predictions of model studies; in both, the total biomass increases (all slopes: $r^2 = 0.64$, $n = 714$, $P < 0.001$; linear regression) and the biomass per period decreases when the wavenumber increases (all slopes: $r^2 = 0.09$, $n = 714$, $P < 0.001$; linear regression). However, a more in-depth inspection reveals disagreements. For one, the effect of ground slope is not strongly present in the data, though its effect is clear in the extended-Klausmeier model (Figure 2.2a). Additionally, the more refined details of wavenumber dependence also differ (it is concave in the theoretical model and convex in the real-life data).

The migration speed is plotted in Figure 2.6 for both the Haud and the Sool sites. These measurements show an increase in speed when the wavenumber decreases (Haud: $r^2 = 0.43$, $n = 104$, $P < 0.001$; Sool: $r^2 = 0.45$, $n = 79$, $P < 0.001$; linear regression), corroborating theoretical predictions (see Figure 2.2b).

5 Discussion

Leading ecological frameworks emphasize the potential role of regular spatial vegetation patterns as indicators for proximity to catastrophic ecosystem shifts [125, 129]. In these frameworks, however, mono-stability of patterns is implicitly assumed, suggesting that for a given environmental condition there is only one stable vegetated state, i.e., a single pattern with a specific wavelength [125, 129]. Subsequent theoretical insights have challenged this view, highlighting the possibility of multi-stability of patterns, bounded by the so-called Busse balloon. In this study, we provide empirical evidence corroborating the existence of a Busse balloon for stable vegetation patterns in dryland ecosystems.

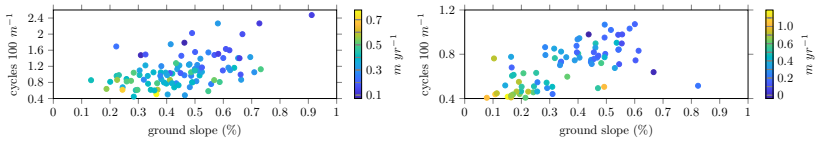

(a) Migration speed (Haud site) **(b)** Migration speed (Sool site)

Figure 2.6: Observed (average) migration speed of vegetation bands in the Haud (a) and the Sool (b) sites over the course of 39 years as a function of ground slope and wavenumber (cycles per 100m). The color gradient indicates the migration speed for a particular (*slope*, *wavenumber*)-combination. The sign indicates the direction of migration relative to the slope, with positive and negative values indicating upslope and downslope migration respectively.

Specifically, our two study sites in Somalia revealed the sustained (i.e., over a 39 year period) co-occurrence of banded vegetation with wavenumbers varying over a substantial range. Our findings have major implications for the way in which vegetation patterns indicate ecosystem resilience and mediate ecosystem responses to environmental change.

Specifically, the existence of a Busse balloon implies that an ecosystem's resilience can no longer merely be defined by the magnitude of environmental change it can cope with [80]. In these systems there is not one tipping point, but a cascade of destabilizations – indicated by the boundary of the Busse balloon. When environmental changes push a patterned ecosystem beyond the boundary of the Busse balloon, a wavelength adaptation occurs, and typically part of the vegetation patches are lost, while the remaining patches grow in size. The extent of these adaptations depends on the rate of environmental change [138, 144–146]. Moreover, human activities or natural variations can cause local disturbances, diminishing the regularity of ecosystem patterns. The recovery process from such disturbances may involve a rearrangement of patches in the landscape [11, 146]. Again, the extent to which such recovery is possible depends on the rate of environmental change that the ecosystem is exposed to [145]. Hence, the existence of a Busse balloon of stable dryland vegetation patterns suggests that adaptability of patches to changing environmental conditions provides a more comprehensive indicator for the ecosystem's resilience than the shape of the pattern itself, as suggested in current leading frameworks [125, 129]. To fully comprehend the consequences of this, it is necessary to provide a more thorough understanding of what determines the spatial rearrangement of vegetation patches resulting from disturbances, environmental changes, and spatial heterogeneities in the landscape.

The pattern-oriented modeling approach was mainly developed to aid model development and design, but the approach can also be used to evaluate the suc-

cess of existing models to explain multiple strong and weak patterns observed [69]. This so-called 'reverse pattern-oriented modeling' approach [69] was used in the current study. Such systematic comparisons between model predictions and empirical data can be part of an iterative process toward further model improvement [93, 94]. In this context, it is interesting to note the discrepancy that we observed between model predictions and field measurements of the influence of the ground slope on pattern migration speeds. Because topography critically changes the distribution of water within ecosystems, it also alters the migration speed of patterns. Therefore, it is of interest to determine the effects of more complex topographies for dryland ecosystem dynamics.

Moreover, the available empirical data aligns with theoretical predictions on both strong and weak patterns. However, environmental conditions were characterized by differences in slope gradient only. Although, indeed, the topography comprised the main source of environmental variation, other less pronounced heterogeneities are present and can cause spreads in wavenumber. The observed spread could not be attributed to variation in rainfall or elevation, but the role of other heterogeneities (e.g. soil composition and grazing activity) could not be fully determined for lack of precise and accurate data sets. When these become more readily available, further research might infer to which extent the observed wavenumber spread is explained by these environmental drivers.

Since their appearance on aerial photographs in the 1950s [102], the origin of regular vegetation patterns in dryland ecosystems has been a topic of fascination within the scientific community. The study of these patterns through reaction-diffusion modeling subsequently highlighted the importance of these patterns for the functioning of dryland ecosystems, and their response to environmental change. The recent increase in the availability of optical and topographical data provides unprecedented opportunities to confront model predictions with empirical data [94, 140]. In this study, we combined these data sources with in-situ measurements of biomass, enabling the comparison of multiple pattern characteristics of Somalia drylands with predictions derived from reaction-diffusion modeling. The empirical evidence corroborates theories of multi-stability of patterned vegetation states, improving our understanding of these systems' resilience to environmental changes. In addition, our results call for more detailed investigations of the role of small-scale topographic variability in pattern formation and migration.

Appendices

2.A Dimensional extended-Klausmeier

The dimensional extended-Klausmeier model is given by (2.A.2). The model used throughout the chapter, equation (2.1), can be obtained from the dimensional version by the right set of scaling. Following [146, Appendix A], the required scaling is given in (2.A.3) for the variables and in (2.A.4) for the parameters of the model.

$$\begin{cases} \dfrac{\partial W}{\partial T} &= E\dfrac{\partial^2 W}{\partial X^2} + \dfrac{\partial (VW)}{\partial X} + A - LW - RWN^2, \\ \dfrac{\partial N}{\partial T} &= D\dfrac{\partial^2 N}{\partial X^2} + RJWN^2 - MN \end{cases} \tag{2.A.2}$$

$$w = \frac{\sqrt{R}J}{\sqrt{L}}W \qquad n = \frac{\sqrt{R}}{\sqrt{L}}N \qquad x = \frac{\sqrt{L}}{\sqrt{D}}X \qquad t = LT \tag{2.A.3}$$

$$a = \frac{\sqrt{R}J}{L\sqrt{L}}A \qquad m = \frac{1}{L}M \qquad v = \frac{1}{\sqrt{LD}}V \qquad e = \frac{E}{D} \tag{2.A.4}$$

In these equations, water is supplied to the system at a rate $+A$, modeling uniform rainfall. Because of evaporation, water is lost at a rate $-LW$; water is also lost through uptake by plants, at rate $-RWN^2$. The parameter J models the increase of biomass per unit of water consumed, which results in the reproduction of plants at rate $+RJWN^2$. Plant mortality is modeled as $-MN$. The parameter V is the speed at which water flows downhill; this is proportional to the slope gradient. Finally, E is the diffusion coefficient of water; D is the diffusion coefficient of vegetation, modeling the dispersal of biomass. See also [90].

2.B Description of study sites

For this study, two sites in Somalia were selected that exhibit mostly banded vegetation. The Haud site is a $35km$ by $28km$ study area (8°0′14″ to 8°15′11″N; 47°11′54″ to 47°31′4″E) at 650-750m elevation in the Haud pastoral region –

see also Figure 2.D.1. Here, banded vegetation dominates the landscape with some minor occurrences of gapped vegetation on flat ground on the summits of rolling hills. Bands display a broad range of wavelengths (from 60m to 200m). Ground slope ranges from 0 to 1%. Mean annual precipitation, ranging from 210mm to 270mm, is distributed in two rainy seasons around spring (April-May) and fall (September-November) separated by two dry seasons. Rainfall data was extracted from Climate Hazards Group InfraRed Precipitation with Stations [59]. Estimates were provided by [35].

In the north-eastern corner of this area near Kalabaydh city, the soils of the bands and inter-bands are very similar [78]. Moreover, the large perennial tussock grass *Andropogon kelleri* dominates the core of the band along with some scattered small trees and bushes [78]. Characteristically, plants are sparsely distributed on the downslope side of the bands. Along this edge and below it, in the bare inter-band, dead trees of all of the species found within the bands were present. Along the bands' upslope side, some initial colonization by two perennial grass species, tussock-forming *Chrysopogon aucheri var. quinqueplumis* and stoloniferous *Dactyloctenium scindicum*, was observed [78]. Although the lifespan of perennial grasses is highly variable, ranging from less than a year to multiple decades [95], the average lifespan of perennial grasses in arid and semi-arid environments is typically 1-7 years [19, 95, 171]. Upon inspection of satellite imageries taken 39 years apart, an upslope migration speed of $0.3m\ yr^{-1}$ was observed [33].

The Sool site is an approximately 77km by 29km study site, located 190km to the NE of the Haud site (9°18′49″ to 9°34′34″N; 48°8′15″ to 48°43′15″E); it is located in the Sool-Plateau pastoral area, which has more arid conditions (100mm-140mm) and higher elevations (900m-1000m) – see also Figure 2.D.1. Here, the ground slope ranges from 0 to 1%, and ground is either bare or covered with banded vegetation which sometimes displays a dashed physiognomy. To the authors knowledge, there is no published record of the composition of these vegetated bands and associated soils. Remote sensing analysis of vegetation dynamic in this area over the last decades have shown a continuous upslope migration of the bands as well as a change in band width. However, no change in wavelength has been observed [33, 66].

2.C Data sets

2.C.1 Topographical data

For both sites, topographical data was retrieved from the ALOS World 3D 30m (AW3D30, v. 2.1) digital raster elevation model. This model describes the height above sea level (in m, rounded to the nearest integer), at a ground resolution of

approximately $30m$ at the equator. The elevation data was preprocessed for the removal of artifacts by applying a global soft-thresholding on its dual tree complex wavelet transform. Specifically, we set a threshold of 0.9 on the first five dual-tree complex wavelet transform levels. From the preprocessed data, we calculated the slope gradient (in %) and slope aspect (in degrees). We first extracted square DEM windows of 33 by 33 cells (i.e., approximately $990m \times 990m$), centered on the image windows. We then applied a least squares fitting procedure of an unconstrained quadratic surface on the unweighted elevation values. From the first derivatives of this fitted surface, evaluated at the focal cell, we could then calculate slope gradient and aspect analytically, following [146]. Complex topographic features were discarded from subsequent analysis by ignoring windows (see below) with quadratic fit RMSE above $1m$ or a total curvature (as defined by [132]) above 10^{-10} radians per m^2.

2.C.2 Biomass measurements

Recently, a map has been made with data on (above-ground) biomass of African savannahs and woodlands at a resolution of $25m$ [15], which provides the biomass data of the patterns studied in this article. This map is built from 2010 L-band PALSAR mosaic produced by JAXA following a method adapted from [105], while the perturbing sources that affect the SAR data have been minimized: the environmental effects (soil and vegetation moisture) were reduced by stratifying the African continent into wet/dry season areas, and the speckle noise inherent to SAR data acquisitions was decreased by applying a multi-image filter developed by [16] that preserves the spatial resolution of the images. Then, the sensitivity of the radar backscatter to AGB was analyzed to develop a direct model relating the PALSAR backscatter to AGB, calibrated with the help of in-situ and ancillary data. The in-situ data were composed of 144 selected field plots, located in 8 countries (Cameroon, Burkina Faso, Malawi, Mali, Ghana, Mozambique, Botswana and South Africa), with plot size larger than $0.25ha$ and a mean plot size of $0.89ha$.

2.C.3 Optical data

Three multi-spectral WorldView-2 images, acquired on December 25th 2011, January 21st 2012 and July 21st 2012, were mosaicked and used as reference orthoimage for the Haud site. For the diachronic study, a panchromatic Ikonos "Geo" imagery, with a $1m$ nominal ground resolution, was used as the reference layer. It was acquired on January 7th 2006. Orthorectification was performed using a rational polynomial coefficient (RPC) camera model block adjustment without ground control points [71].

A mosaic of six WorldView-2 images, acquired between February 3rd 2011 and September 12th 2013, was used for the Sool sites. For the diachronic study,

a panchromatic SPOT4 image preprocessed to level 2A, with a $10m$ nominal ground resolution, was use as reference layer (©Cnes 2004 – Spot Image distribution). It was acquired on February 18th 2004.

Two $7\mu m$ digitized panchromatic declassified Corona spy satellite image, national intelligence reconnaissance system, available from the USGS, were acquired on February 28th 1967 (KH-4A, mission 1039, AFT camera) and December 12th 1967 (KH-4B, mission 1102, FWD camera), respectively for the Haud and the Sool. The images were co-registered with the orthorectified reference imagery. Co-registration was performed using a third-order polynomial adjustment using landmarks such as geological features, crossroads, isolated trees, or large termite nests. We obtained an RMS adjustment error below the KH-4A ground resolution, which is $3m$ for this area. The resolution of the imagery was then lowered through pixel averaging to match the coarsest image pair.

The analysis of pattern wavelength was performed over the full area of the study sites. However, for the diachronic study, a subset of each of the sites covered by the historic and reference image was selected. Projection and datum for all data sets were WGS 1984, UTM Zone 38N and 39N respectively for the Haud and the Sool sites.

2.D Data processing

2.D.1 Spectral analysis, direction of anisotropy and wavelength

On visible light digital images over drylands, bright pixels correspond to bare soil, intermediate gray-scale levels to closed grass cover, and darker pixels to woody vegetation. As a first approximation, gray-scale levels can thus be considered as a monotonically decreasing function of the above-ground biomass [28]. This approximation allows us to analyze the spatio-temporal dynamics of biomass organization through image analysis techniques.

We used a Fourier windowing technique equivalent to short time Fourier transforms to obtain spatial maps of dominant pattern wavelength λ and orientation θ from the satellite images as previously used for banded vegetation systems [7, 27, 34, 118]. We applied a two-dimensional (2D) Fourier transform to obtain the power spectrum within square, non-overlapping moving windows. In order to maintain resolution and signal-to-noise ratio a boxcar windowing function to signal was applied. This choice is, in this case, reasonable as only one periodic component is expected to be present in the vegetation. The technique provides information about the local wave-vector $k = k_x\hat{x} + k_y\hat{y}$. The two-dimensional (2D) fast Fourier transform $\tilde{f}(k_x, k_y)$ of the pattern of biomass

$f(x, y)$ was obtained for each window $\tilde{f}(k)$ of size $L \times L$. As L increases, the spatial resolution, i.e., localization in space of frequency or orientation change, is reduced. Conversely, as L decreases, the frequency resolution is decreased, i.e., the likelihood of separating frequency components close together in Fourier space. To optimize both, L was chosen to be at least 3λ, i.e., $750m$ and $1010m$ respectively for the Haud and the Sool sites.

To separate the characteristics of the signal that are meaningful for this study, each k, of frequency $2\pi/\lambda$ (wavenumber), was decomposed into its orientation θ and its magnitude. For each window, the power spectrum $S(k) = |\tilde{f}(k)|^2$ was computed. The power spectrum measures how the variation, or power, of the pattern is distributed over the wavevectors k, of different frequencies and spatial directions. To identify the dominant k in each window, $S(k)$ was binned into annular rings of unit width [123]. The resulting radial spectrum thus quantifies the contribution of successive ranges of spatial frequencies to the image variance across all orientations.

To deconvolve the natural $1/k$ scaling of the power spectrum, the total power within each annular ring, $S(k)$, was computed instead of the mean power. The location peak of this total power is used to define the most energetic wavenumber, k_1. To compensate for the discrete k-resolution in Fourier space, the location of the weighted average $k_1 := (\sum_k kS(k)) / (\sum_k S(k))$ was computed over all rings that formed part of the peak and contained more than 70% of the peak power.

The patterns were characterized in terms of level and orientation of anisotropy (i.e., direction orthogonal to the long axis of the bands) following [34]. The average pattern orientation was studied using the circular mean direction weighted by the power spectrum values, $\bar{\theta} := \frac{1}{2}\arctan2(S, C)$, where

$$S := \left(\sum_k 2k_{x,y} \sin\theta_{x,y}\right) / \left(\sum_k k\right)$$

and

$$C := \left(\sum_k 2k_{x,y} \cos\theta_{x,y}\right) / \left(\sum_k k\right).$$

The norm of the resultant vector, $\bar{R} := \sqrt{S^2 + C^2} / (\sum_k k)$, was used as an index of pattern anisotropy. The division by the sum of periodogram amplitudes ensures bounding between zero (perfect isotropy) and one (all variance concentrated in one direction, i.e., perfect bands). Pattern orientation features were extracted from the power spectrum, within the frequency ring characterizing periodic vegetation patterns, i.e., between 0.4 and 2.5 cycles $100m^{-1}$ for both the Haul and the Sool site, to exclude anisotropy sources resulting from large scale gradients or small scale (anthropogenic) features.

2.D.2 Pattern classification

The vegetation cover of each window was quantified by converting the gray-scale intensity image to a binary image using the Otsu thresholding method [116]. Windows with less than 15% vegetation cover were considered as bare soil and discarded. Windows with dominant patterns within the acceptable range (i.e., between 0.4 and 2.5 cycles $100m^{-1}$ for both sites) and with anisotropy index above 0.2 were considered as banded patterns.

2.D.3 Cross-spectral analysis and migration speed

Scale specific comparisons between pairs of periodic 2D signals – in this case, images taken at different dates – can be performed through 2D Fourier cross-spectral analysis. In principle, this means identifying the frequencies and orientations of patterns dominating in any two images as well as possible shifts among them. Correction of radiometric variability between dates is not required since Fourier coefficients are invariant to linear rescaling of gray-scale levels. A detailed mathematical development of the analysis can be found in [8]. The procedure can be summarized as follows [33, 66].

To assess band migration distance for each temporal pair of image windows, a coherency spectrum and a phase spectrum were computed. The coherency spectrum expresses the correlation between the frequency components of the Fourier spectra of the pair of windows. For each spatial frequency, the coherency value is interpreted in a similar way to the classical Pearson's coefficient but in absolute values, because the sign of the correlation is expressed by the phase spectrum. For each window pair, the maximum value of coherency and its associated frequency were recorded along the direction of maximal anisotropy computed for the first acquisition date. Window pairs with a maximum coherency below 0.9 were rejected from the analysis, because this indicates that pattern characteristics (wavelength and orientation) changed between the dates. Rejected windows often corresponded to man-made perturbations or ephemeral patterns, which are not the subject of this study. The obtained frequency value therefore corresponds to a pattern of constant scale and orientations dominating at both acquisition dates. The corresponding phase-spectrum value provides the phase difference, i.e., the angular distance, between the selected frequency components at both dates in the maximal anisotropy direction. This value is defined between -180 and 180 degrees, with the sign representing the forward (+) vs. backward (−) displacement, with the direction of reference as the upslope direction. Angular distances were then converted into meters by multiplying the phase difference by the wavelength, which in turn were converted to an average migration speed for the time period. This conversion allows for inter-site comparisons independent of varying time intervals. An inherent limitation to this procedure is that only migration distances not exceeding half the wavelength

will be correctly estimated (phase saturation). This condition was verified by visual inspection prior to image analysis.

2.D.4 Assessment of uncertainty in calculations of slope gradient and aspect from topographical data

As the digital raster elevation model contains errors, these will propagate into derived estimates of slope gradient and aspect. Ideally, one would use ground observations (e.g. using differential global navigation satellite systems) to assess the magnitude of these errors (e.g. [119]). Since such observations are not available for our study areas, we used a simulation method to evaluate the propagation of error from the elevation data to the estimates of slope gradient and aspect. Specifically, we created artificial elevation grids with a fixed (from here referred to as 'true') slope and aspect, and added to these grids (normally distributed) random errors with a similar standard deviation as observed in the AW3D30 dataset. The resulting elevation values were rounded to the nearest integers, as this is also done in the AW3D30 dataset. Then, utilizing the same procedures as described above (see section 2.C2.C.1), we derived slope gradients and aspects from these simulated grids. Comparison of this 'observed' slope and aspect and the 'true' slope and aspect of the grid yielded insight in the propagation of errors from the elevation model to the calculated metrics. Seven fixed slope levels were considered: 0; 0.025; 0.05; 0.1; 0.2; 0.3 and 0.4%. For each level, we simulated $10,000$ replicate grids of errors that were added to the fixed slope level. For each replicate, the aspect was a randomly assigned value between 0 and 360 degrees.

Following the above procedure, we found that the distributions of errors in the calculated slope gradients and aspects were relatively small, for all slope levels considered (Figure 2.D.3). Because the estimated slope is bounded between zero and positive infinity, a small positive bias was observed for slopes less than 0.1%. For slopes of 0.025% and higher, the RMSE is 0.010% and 95% of the observed errors for slopes of 0.1% or higher are within ± 0.016% (5^{th} and 95^{th} percentiles). For aspect, the magnitude of errors was inversely proportional to the magnitude of the slopes (abscissa; Figure 2.D.3). For slopes of 0.2% and higher, the RMSE is 2.9 degrees or lower, and 95% of the observed errors are within ±4.8 degrees (5^{th} and 95^{th} percentiles). These results show that the errors in calculated slopes and aspects were relatively small compared to the observed range in the dataset. Hence, it is unlikely that correlations between pattern metrics and slope gradients, as observed in the main text, are strongly affected by the errors originating from the underlying topographical database.

Moreover, it should be noted that the above procedure may even be overestimating the errors associated with the AW3D30 dataset (from here referred

to as the 30m elevation dataset). To generate the simulated errors, we used the global average standard deviation of the difference between the original AW3D 5m elevation dataset (from here referred to as the 5m dataset), from which the 30m dataset has been derived, and a reference LiDAR dataset. This standard deviation is 1.73m for gently sloping terrain (below 17.6%) [148]. However, as the 30m elevation dataset was produced by averaging non-overlapping windows of 7 by 7 pixels of the 5m elevation dataset, the resulting standard deviation will be lower [147]. Additionally, the ground slope in our study areas is at the lower end of the 0-17.6% range, namely below 1.5%, and therefore likely to suffer from smaller errors than reported for the whole range. Finally, the Somalian area we are studying displays relatively small errors in elevation measurements compared to other areas of the world [148].

2.D.5 Assessment of uncertainty in estimation of pattern frequency from optical imagery

The estimation of the dominant pattern frequency using a Fourier windowing technique introduces an unknown uncertainty in these estimations. This uncertainty stems from the decomposition of the signal into a discrete set of frequencies and from the noise in the analyzed (non-stationary) signal. To asses the model's uncertainty in the wavenumber estimations, we have used a simulation method. Specifically, we simulated 200 synthetic images, representing a two-dimensional sinusoid of each frequency class between 0.4 and 2.4 cycles $100m^{-1}$, with step size of 0.2. The directions of the sinusoidal waves were selected randomly and the signal was standardized to have zero mean and standard deviation of one. To mimic real images of vegetation patterns, we have added red noise with zero mean and standard deviation of 0.5 to each simulated signal. Red noise is a self-similar, or fractal, random spatial structure; this is a desirable property here because these are common in nature and especially in natural landscapes [89]. The noise was created using the Fourier synthesis technique with an energy spectrum exponent of 0.5 [36]. Finally, in order to account for the fact that reflectance values are constant over the width of both vegetated and bare bands, the signal was converted to binomial values; that is, values between 0 and 1 were rounded to the nearest integer value. Several examples of simulated bands are presented in Figure 2.D.5.

Using the characteristics of the optical image windows of the Haud site (cell-size of 2.36m and windows 317 by 317 cells), the root-mean-square error of the estimated frequency was 0.082 cycles $100m^{-1}$. For the Sool (cell-size of 2.36m and windows 425 by 425 cells), the root-mean-square error was 0.044 cycles $100m^{-1}$. The magnitude of this error is significantly less than the observed variability in frequency in both sites (for every slope bin of Figure 3 in the main text, Levene's test, $P < 0.001$), showing significance of the observed

wavenumber spread in both study sites.

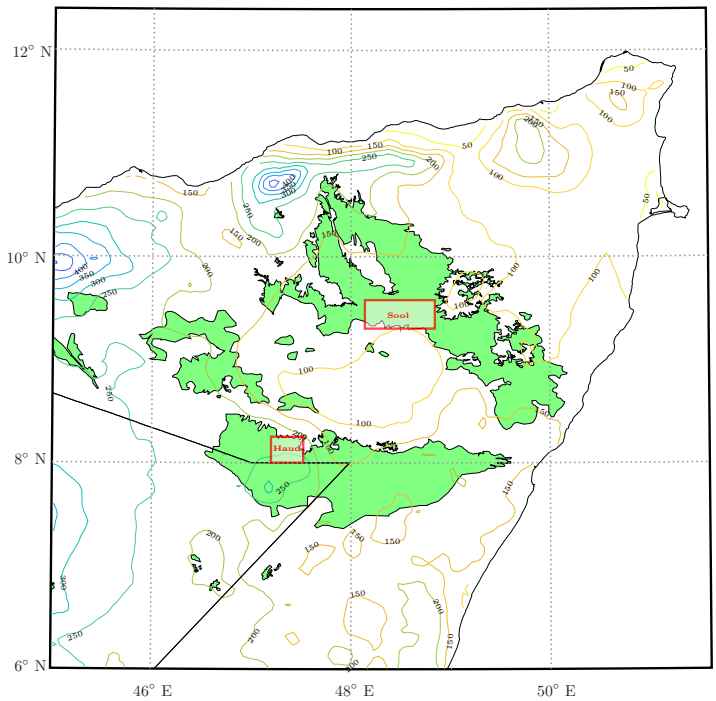

Figure 2.D.1: Locations of the study sites and rainfall gradient in the Horn of Africa. The 'Haud' site (8°0′14″ to 8°15′11″N; 47°11′54″ to 47°31′4″E) has a mean annual rainfall of 210–270*mm* yr^{-1} whilst the 'Sool' site (9°18′49″ to 9°34′34″N; 48°8′15″ to 48°43′15″E) has a mean annual rainfall of 100–140*mm* yr^{-1}. The distribution of periodic vegetation pattern shown in green is adapted from [32]. Precipitation data was extracted from Climate Hazards Group InfraRed Precipitation with Stations [59] and is averaged over the years 1981–2013.

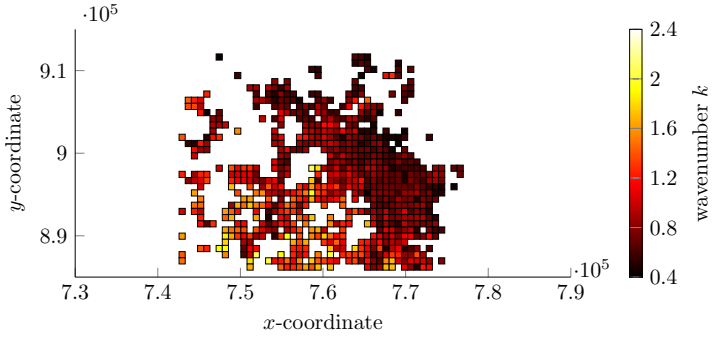

(a) Haud site

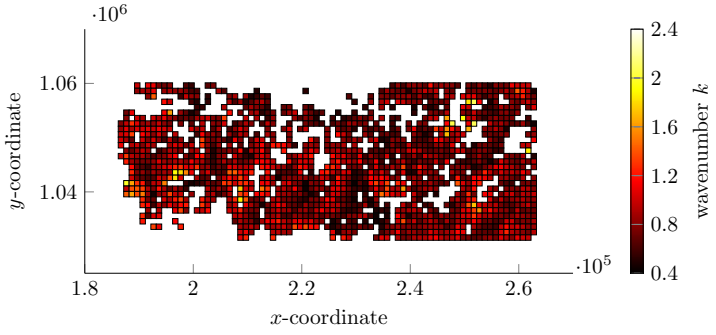

(b) Sool site

Figure 2.D.2: The distribution of the measured banded pattern's wavenumber over the Haud site (a) and the Sool site (b). Here, darker red indicates a lower wavenumber and lighter yellow a higher wavenumber. On the x- and y-axes the UTM coordinates of the locations are given.

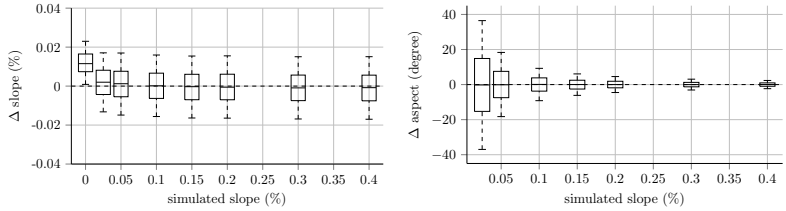

(a) Estimated slope error **(b)** Estimated aspect error

Figure 2.D.3: Slope (a) and aspect (b) estimation error from simulated topographical surfaces. Median errors are shown as horizontal bars with 25$^{\text{th}}$-75$^{\text{th}}$ percentile ranges (boxes) and 5$^{\text{th}}$ and 95$^{\text{th}}$ percentile outlier cutoffs (whiskers). Note that aspect error could range from -180 to $+180$ degrees but has been cropped to largest measured error for visual purpose.

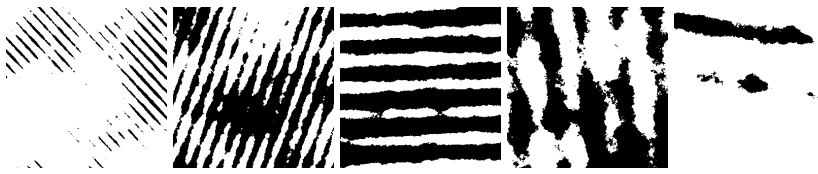

Figure 2.D.4: Examples of simulated vegetation patterns with frequency decreasing from left (2.4 cycles $100m^{-1}$) to right (0.4 cycles $100m^{-1}$).

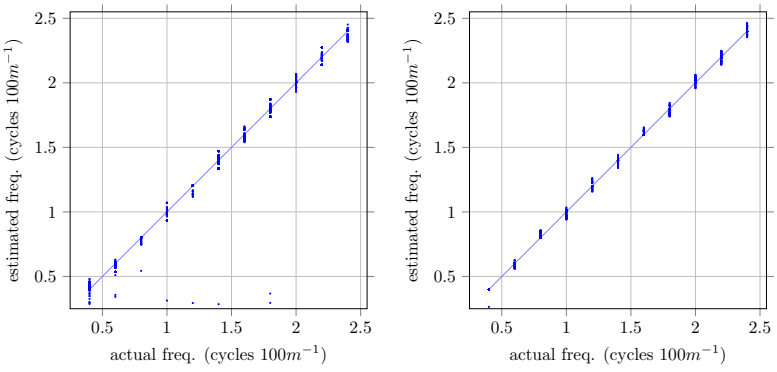

(a) Haud site **(b)** Sool site

Figure 2.D.5: Pattern frequency estimation error for the Haud (a) and the Sool (b) sites. Actual frequency of the simulated patterns and the corresponding estimation of these frequencies is shown by the blue dots. The straight line represents the perfect estimation line.